ARTICLE IN PRESS

Journal of Crystal Growth ∎ (∎∎∎∎) ∎∎∎–∎∎∎

Contents lists available at ScienceDirect

Journal of Crystal Growth

journal homepage: www.elsevier.com/locate/jcrysgro

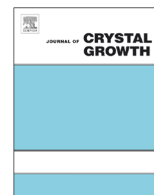

Morphology and arrangement of InN nanocolumns deposited by radio-frequency sputtering: Effect of the buffer layer

L. Monteagudo-Lerma [a], S. Valdueza-Felip [b,c], A. Núñez-Cascajero [a], A. Ruiz [d], M. González-Herráez [a], E. Monroy [b,c], F.B. Naranjo [a]

[a] Grupo de Ingeniería Fotónica, Departamento de Electrónica, Universidad de Alcalá, Ctra. Madrid-Barcelona km. 33.6, 28871 Alcalá de Henares, Madrid, Spain
[b] University Grenoble-Alpes, 38000 Grenoble, France
[c] CEA, INAC-SP2M, 17 av. des Martyrs, 38000 Grenoble, France
[d] Instituto de Ciencia de Materiales de Madrid, CSIC, Sor Juana Inés de la Cruz, 3, 28049 Madrid, Spain

ARTICLE INFO

Article history:
Received 1 September 2015
Received in revised form
7 October 2015
Accepted 19 October 2015
Communicated by Prof. J.M. Redwing

Keywords:
A1. Atomic force microscopy
A1. Nanostructures
A1. X-ray diffraction
A3. Sputtering
B2. Semiconducting indium nitride

ABSTRACT

We present the structural and optical properties of (0001)-oriented nanocolumnar films of InN deposited on *c*-sapphire substrates by radio-frequency reactive sputtering. It is observed that the column density and dimensions are highly dependent on the growth parameters of the buffer layer. We investigate four buffer layers consisting of (i) 30 nm of low-growth-rate InN, (ii) 30 nm of AlN deposited on the unbiased substrate (us), (iii) 30 nm of AlN deposited on the reverse-biased substrate (bs), and (iv) a 60-nm-thick bilayer consisting of 30-nm-thick bs-AlN deposited on top of 30-nm-thick us-AlN. Differences in the layer nucleation process due to the buffer layer induce variations of the column density in the range of $(2.5–16)\times 10^9\ cm^{-2}$, and of the column diameter in the range of 87–176 nm. Best results in terms of mosaicity are obtained using the bs-AlN buffer layer, which leads to a full width at half-maximum of the InN(0002) rocking curve of 1.2°. A residual compressive strain is still present in the nanocolumns. All samples exhibit room temperature photoluminescence emission at ~1.6 eV, and an apparent optical band gap at ~1.7 eV estimated from linear optical transmittance measurements.

© 2015 Published by Elsevier B.V.

1. Introduction

InN research has raised considerable interest for the development of optical coatings, low-resistance ohmic contacts, and optoelectronic devices such as solar cells or opto-chemical sensors [1,2], due to its room temperature direct optical band gap in the near-infrared (NIR) range (E_g~0.7 eV) [1], high electron mobility and radiation resistance. High-quality InN has been grown mainly by molecular beam epitaxy (MBE) [3–6] and metalorganic vapor phase epitaxy (MOVPE) [7–9]. The optimal substrate temperature (T_s) for InN growth is close to the decomposition temperature of the material, around 500 °C [10]. In the case of MBE, the indium desorption rate at the InN growth temperature should be negligible, which reduces drastically the growth window. In MOVPE, the relatively low growth temperature of InN results in wetting-related problems and difficulties to crack NH_3. Radio-frequency (RF) reactive sputtering emerges as a suitable and low-cost technique for thin film growth at lower temperature, even at room temperature, and on a wide range of rigid (glass, silicon, sapphire, GaN-on-sapphire [11–14]), and flexible [15–17] substrates.

It is known that usually the insertion of an AlN buffer layer leads to an improvement of the subsequent III-nitride crystalline quality, which is valid also for RF reactive sputtering technique [18–21]. It has also been reported that biasing the substrate can lead to an improvement of the structural quality of RF-sputtered AlN through an increase in the kinetic energy of the impinging ions [22]. In this work, we investigate the influence of biasing the AlN-on-sapphire buffer layer on the nanostructure of the InN films deposited on top by RF reactive sputtering. Results on unbiased AlN (us-AlN) and biased AlN (bs-AlN) buffer layers are compared to those obtained using a low-growth-rate InN buffer layer on sapphire [23].

2. Experimental

The InN samples under study were deposited on (0001)-oriented sapphire substrates using an RF reactive sputtering system (AJA International, ATC ORION-3-HV) equipped with a 2 in. confocal magnetron cathode. The In and Al targets were of 4N5 and 5N purity, respectively, whereas the reactive gas was 6N pure N_2. The

E-mail address: laura.monteagudo@depeca.uah.es (L. Monteagudo-Lerma).

http://dx.doi.org/10.1016/j.jcrysgro.2015.10.016
0022-0248/© 2015 Published by Elsevier B.V.

ARTICLE IN PRESS

Table 1
Description of the samples under study: nature and thickness of the buffer layer, FWHM of the InN(0002) rocking curve, column density, columns diameter, rms surface roughness and growth rate of the InN films.

	S1	S2	S3	S4
Buffer	InN	us-AlN	bs-AlN	Double AlN (us-AlN+bs-AlN)
Buffer thickness (nm)	30	30	30	60
FWHM InN(0002) rocking curve (°)	2.4	1.5	1.2	2.7
Column surface density (cm^{-2})	2.5×10^9	3.7×10^9	–	16×10^9
Column diameter (nm)	176 ± 20	170 ± 25	–	87 ± 9
rms surface roughness (nm)	71	49	32	6
Growth rate (nm/h)	100 ± 14	114 ± 16	80 ± 7	178 ± 13

distance between both targets and the substrate was set to 10.5 cm. In order to monitor the substrate temperature during the deposition process, a K-type thermocouple was placed in contact with the substrate holder. Prior to growth, the substrates were chemically cleaned in organic solvents and blown dry with nitrogen. The substrates were outgassed in the deposition chamber for 30 min at a substrate temperature $T_s=550$ °C (100 °C above the growth temperature). The base pressure before growth was $\sim10^{-5}$ Pa. The targets were pre-sputtered with 5N pure Ar plasma.

The deposition of the AlN- and InN-buffers and the InN layers was performed in pure nitrogen atmosphere, under a sputtering pressure of 0.47 Pa and at a substrate temperature of 450 °C. The InN layers were deposited using an RF power $P_{RF}=40$ W with the sample holder unbiased. For deposition of the bs-AlN layer the substrate bias was tuned using a DC voltage source connected to the substrate holder through a resistor (56.2 Ω) with the deposition chamber electrically grounded. As summarized in Table 1, four different buffer layers were considered:

- S1: 30-nm-thick low-growth-rate InN buffer layer grown with $P_{RF}=20$ W (deposited at 60 nm/h) and with the sample holder unbiased, following the growth conditions described in Ref. [23];
- S2: 30-nm-thick AlN buffer layer grown at $P_{RF}=150$ W with the sample holder unbiased (us-AlN);
- S3: 30-nm-thick AlN buffer layer grown at $P_{RF}=150$ W with the sample holder biased at −15 V (bs-AlN). This bias value was previously optimized for the deposition of RF sputtered AlN films [22];
- S4: a double AlN buffer layer consisting of 30 nm of us-AlN followed by 30 nm of bs-AlN. This growth sequence was formerly reported to provide the best crystalline quality of RF sputtered AlN [22].

Structural properties such as crystal orientation, grain alignment and lattice constants were investigated by high-resolution x-ray diffraction (HRXRD) using a four-axis Bruker AXS D8 Advance diffractometer. This structural characterization was based on symmetric $2\theta/\omega$-scans spanning the sapphire(0006) and InN(0002) reflections, as well as InN(0002) rocking curves, and reciprocal space maps around the symmetric (0002) and the asymmetric (−1015) x-ray reflections of InN. The surface morphology of the layers was analyzed by atomic force microscopy (AFM) in the tapping mode using a Veeco Dimension 3100 microscope. Data visualization and processing were carried out with the WSxM software [24]. The morphology and the thickness of the layers were studied by field emission scanning electron microscopy (FESEM) using a Zeiss Ultra 55 microscope.

The optical properties of the films were analyzed by linear optical transmittance and photoluminescence (PL) experiments at room

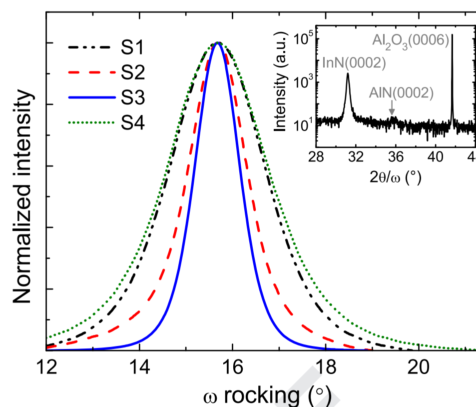

Fig. 1. HRXRD ω-scans of the (0002) x-ray reflection peak of InN layers deposited using the different buffer layers under study (S1–S4). Inset: typical HRXRD $2\theta/\omega$-scan of a representative InN sample deposited with AlN buffer, showing (0001) preferred growth orientation.

temperature. Transmittance measurements were performed under normal incidence in the visible/NIR spectral range (350–1700 nm) using an optical spectrum analyzer. The excitation source for PL measurements was provided by an InGaN laser diode ($\lambda=405$ nm). The excitation power was 7 mW, focused onto a 50-μm-diameter spot. The sample emission was collected into a 45-cm-focal-length Jobin-Yvon monochromator and detected by a charge-coupled-device (CCD) camera.

3. Results and discussion

All the investigated InN layers present wurtzite crystallographic structure with (0001)-preferred growth orientation, as deduced from HRXRD $2\theta/\omega$-scans (see the inset of Fig. 1 as an example). A weak peak at $2\theta\sim36°$, attributed to the AlN(0002) reflection is observed in the samples with AlN buffer layer. Fig. 1 shows the ω-scan of the InN (0002) reflection of samples grown with different buffer layers. A remarkable improvement of the InN crystal quality is obtained when using a single 30-nm-thick AlN buffer layer (samples S2 and S3) compared to the use of the low-growth-rate InN buffer layer (sample S4). As summarized in Table 1, the full-width at half-maximum (FWHM) values of the InN(0002) rocking curve decreases from 2.4°, when using the low-growth-rate InN buffer layer, to 1.5° and 1.2°, in the case of us-AlN and bs-AlN buffer layers, respectively. The upgrade of the crystalline quality of negatively-biased AlN layers has been previously reported, being attributed to an increase of the kinetic energy of the species reaching the growing surface [22,25]. Thereby, the enhanced structural properties of the bs-AlN-based buffer layer, compared to us-AlN, results in a better crystal quality of the subsequent InN film. On the contrary, a clear degradation is obtained when using a double AlN buffer, increasing the FWHM of the InN (0002) rocking curve up to 2.7°.

To get a deeper view into the structural changes induced by the different buffer layers, AFM measurements were carried out. Fig. 2 displays 2×2 μm² AFM images of the samples under study, and the extracted values of root-mean-square (rms) surface roughness are tabulated in Table 1. AFM images reflect a nanostructured morphology, with a decrease of the diameter of the nanostructures by a factor of 2 (from 176 ± 20 to 87 ± 9 nm), and an increase of its density from 2.5×10^9 to 16×10^9 cm^{-2}, for InN grown on the double AlN buffer layer (S4), compared to the material grown on the InN buffer (S1). Accordingly, the rms surface roughness decreases from ∼71 nm for sample S1 to ∼6 nm for S4.

The best result in terms of the lowest rms surface roughness is obtained for sample S4, which also presents the broadest x-ray

ARTICLE IN PRESS

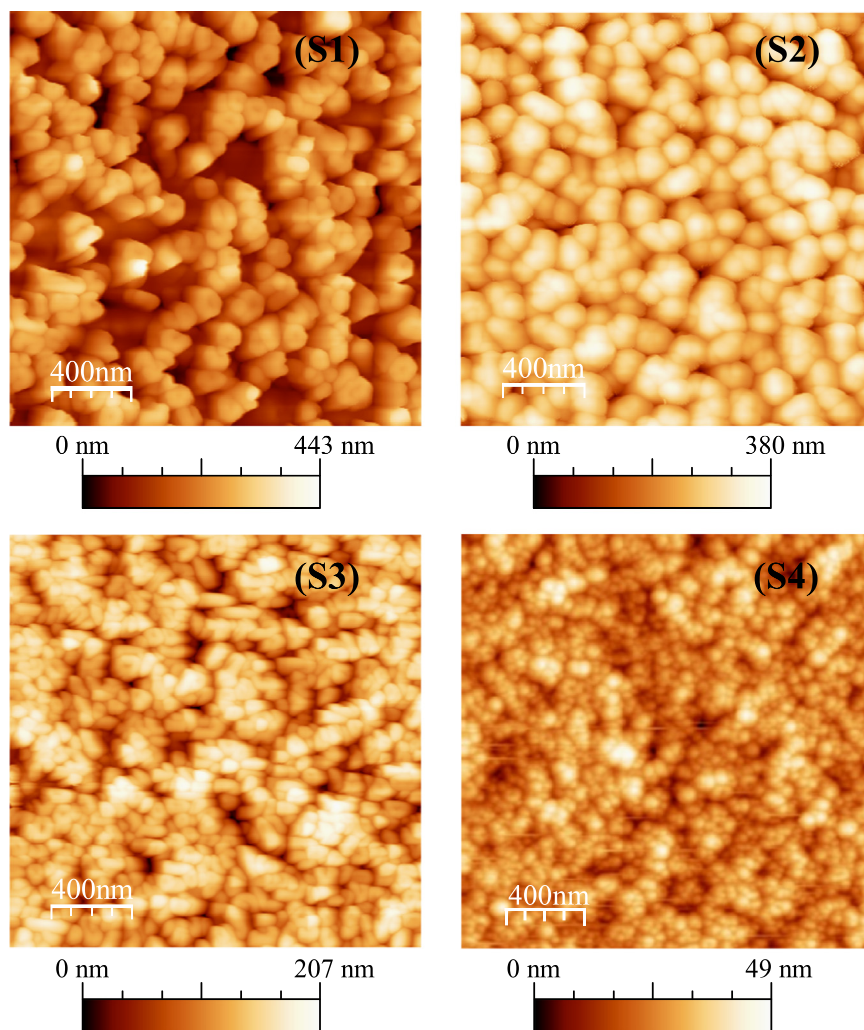

Fig. 2. AFM images ($2 \times 2\ \mu m^2$ scan area) of the InN layers under study (S1–S4).

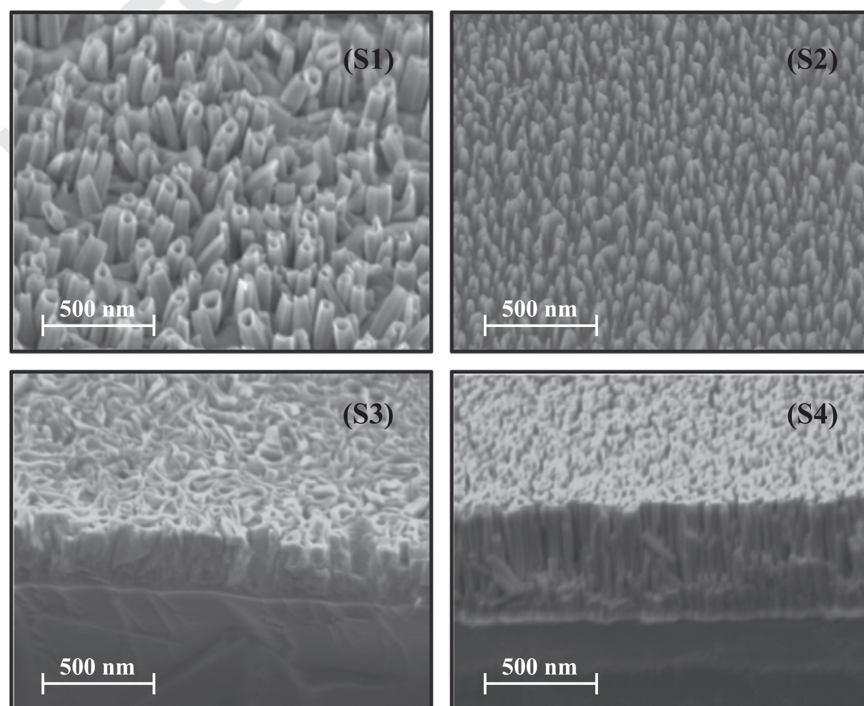

Fig. 3. 45° tilted FESEM images of all the InN layers under study.

Please cite this article as: L. Monteagudo-Lerma, et al., Journal of Crystal Growth (2015), http://dx.doi.org/10.1016/j.jcrysgro.2015.10.016

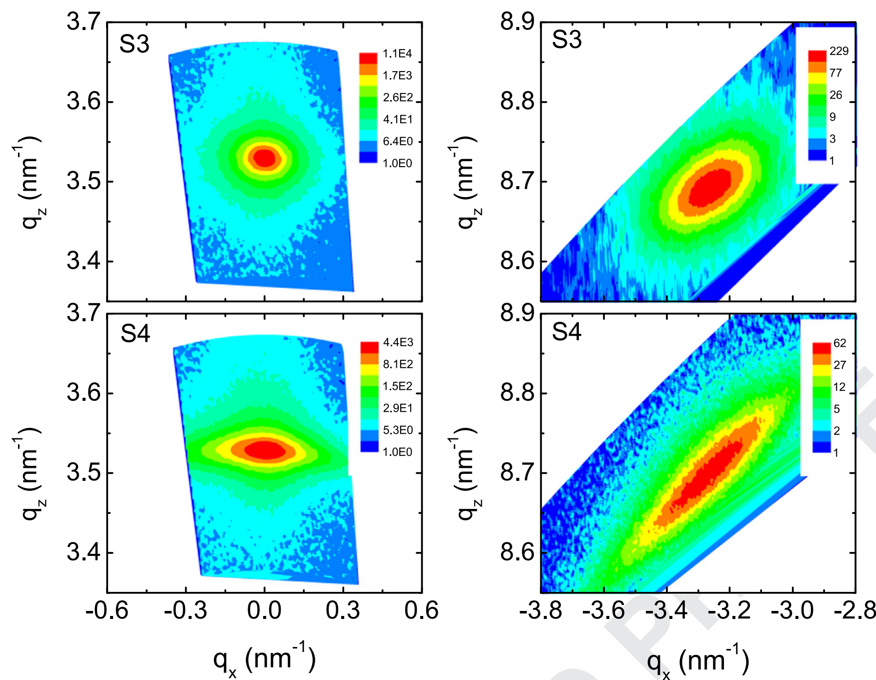

Fig. 4. Reciprocal space maps of the (0002) symmetric reflection [left] and the (− 1015) asymmetric reflection [right] for samples S3 (top) and S4 (bottom).

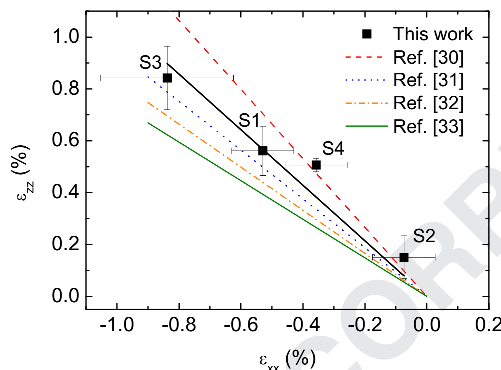

Fig. 5. Out-of-plane strain ϵ_{zz} as a function of the in-plane strain ϵ_{xx} for samples S1–S4. Lines represent the proportionality deduced from elastic constant values reported by other authors.

rocking curve in Fig. 1. For a better understanding of these results, we have studied the samples by FESEM. Images in Fig. 3 of the surface and cross section of the samples viewed with a 45°-tilt confirm the nanocolumnar morphology of the InN layers for samples S1, S2 and S4. In contrast, sample S3 presents an almost compact structure with rough surface morphology, indicative of a 3D growth front. The columnar growth type present in the layers is then attributed to the used slightly N-rich growth conditions, as it is confirmed by the larger InN deposition rate obtained for columnar-mode growth compared to the almost compact InN sample (S3) (see Table 1). This columnar deposition could be hindered by the increase of the nucleation points density when using a biased AlN buffer which induces initial lattice disorder at the interface AlN–sapphire [22] enabling, in turn, the grain coalescence. This behavior has been also observed in InN layers grown on GaN-templates, in which a change in the nucleation layer could lead to a structural change in InN with its morphology evolving from columnar to compact [26]. On the other hand, columnar growth offers larger possibilities of variation of the tilt, thereby leading to structures with larger FWHM of the InN(0002) rocking curve, increasing for columns with smaller diameter (S4). Both crystal quality and column dimensions shown in the obtained samples are similar to other samples grown by MBE [27].

Fig. 4 shows the reciprocal space maps, in reciprocal lattice units (q_x, q_z), obtained around the InN(0002) symmetric reflection and the InN(− 1015) asymmetric reflection for samples S3 and S4, i. e., the most compact InN layer within the studied layers and the structure with smaller nanocolumns, respectively. The enhanced tilt in the nanocolumnar structure (S4) leads to a broadening of the x-ray reflections in the ω-scan direction for both symmetric and asymmetric analyzed reflections, in comparison to the compact sample (S3).

The a and c lattice constants are calculated from the reciprocal space maps through the expressions: $a=\frac{2h}{(\sqrt{3}q_x)}$ and $c=\frac{l}{q_z}$, respectively, where h and l denotes the first and the fourth Miller indices of the considered reflection, and q_x and q_z correspond to the reciprocal space coordinates of the reflection peak. Fig. 5 displays the calculated in-plane $\varepsilon_{xx}=\frac{a-a_o}{a_o}$ and out-of-plane $\varepsilon_{zz}=\frac{c-c_o}{c_o}$ strain for each sample, considering $a_0=3.545$ Å and $c_0=5.703$ Å as the lattice constants for relaxed InN at room temperature [28]. The highest value of residual compressive strain is $\varepsilon_{zz}=(0.84\pm0.12)$% being obtained for the most compact sample (S3), as it has been observed by other authors [26]. In the case of biaxial strain in a hexagonal system, the relationship between ε_{xx} and ε_{zz} is given by:

$$\frac{\epsilon_{zz}}{\epsilon_{xx}}=-2C_{13}/C_{33} \tag{1}$$

where C_{13} and C_{33} are the components of the elastic stiffness tensor [29]. The $\frac{\epsilon_{zz}}{\epsilon_{xx}}$ ratios of all the samples under study are within the range from 0.74 to 1.33 obtained from the values of the theoretical and experimental elastic coefficients reported in the literature for wurtzite InN layers [30–33] (lines in Fig. 5).

The results of the optical characterization of the samples are summarized in Table 2. Fig. 6 depicts the squared absorption coefficient (α^2) of samples S3 and S4 measured at room temperature. The value of α has been derived from optical transmittance (Tr) measurements using $\alpha(\lambda)\propto$ -ln(Tr), which neglects losses introduced by optical reflection at interfaces and optical scattering. The apparent optical band gap energy, $E_{g,opt}$, is estimated by the extrapolation to the x-axis of the linear fit of the α^2 plot as a function of energy. In all cases, $E_{g,opt}$ is in the range of 1.71 ± 0.04 eV, similar [34] or smaller [35,36]

UNCORRECTED PROOF

Please cite this article as: L. Monteagudo-Lerma, et al., Journal of Crystal Growth (2015), http://dx.doi.org/10.1016/j.jcrysgro.2015.10.016

ARTICLE IN PRESS

Table 2
Summary of optical characterization results obtained using transmittance and PL measurements.

	S1	S2	S3	S4
$E_{g,opt}$ (eV)	1.746	1.714	1.715	1.690
ΔE (meV)	115	148	130	174
E_{PL} (eV)	1.557	1.561	1.583	1.666
FWHM E_{PL} (meV)	301	355	302	415
Stokes-shift (meV)	189	153	132	24

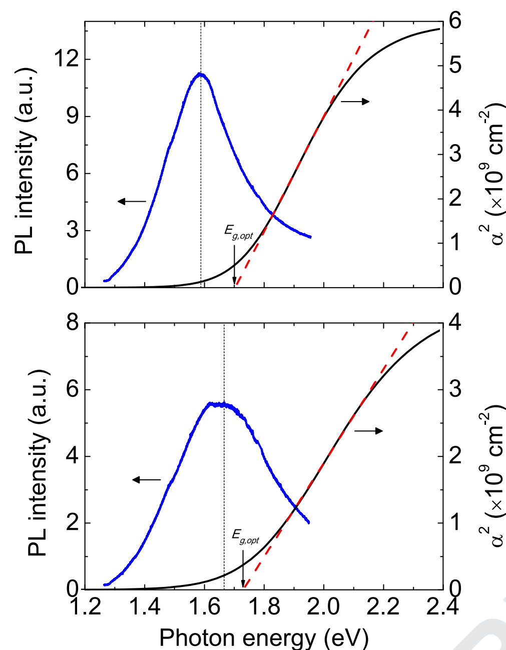

Fig. 6. Room temperature PL emission spectra and squared absorption coefficient (solid line) with a linear fit (dashed line) as a function of the photon energy for samples S3 and S4.

than values reported by other authors in InN samples deposited by reactive sputtering. However, these values of $E_{g,opt}$ are still much larger than the ~0.64 eV reported for high-quality single-crystalline InN grown by MBE or MOVPE [2]. The large $E_{g,opt}$ in sputtered InN samples has been widely discussed in the literature and is generally attributed to its polycrystalline nature and the Burstein–Moss effect associated to their high residual carrier concentration. From our measurement of $E_{g,opt}$, the free carrier concentration is estimated to be in the range of mid-10^{20} cm^{-3} [37], in agreement with the residual carrier concentration obtained through Hall measurements in similar InN compact samples deposited by RF sputtering [23].

Fig. 6 also shows the room-temperature PL emission spectra for samples S3 and S4. For all the InN films under study the PL peak energy is located at $E_{PL}=1.59\pm0.08$ eV, and presents a FWHM larger than 300 meV, as summarized in Table 2. Samples from S1 to S3 show similar optical features, with absorption edge broadening in the range of (130 ± 18) meV, and Stokes-shift from 130 to 190 meV (see Table 2), in agreement with results presented by other authors [1]. These large Stokes-shifts together with the high FWHM of the PL emission can be attributed to emission from potential fluctuations due to a non-homogeneous distribution of defects [38]. Particularly, the Stokes-shift value for columnar InN samples decreases with the nanocolumn diameter. In the case of S4, the smaller Stokes-shift (24 meV) is associated with the highest PL emission energy and the highest FWHM of the PL peak among the analyzed samples. This is probably related to the significant reduction of the nanocolumn diameter, which could lead to a higher influence of nanocolumn diameter dispersion [39].

4. Conclusions

We have presented a study of the influence of the buffer layer on the structural, morphological and optical properties of (0001)-oriented nanocolumnar InN layers deposited on sapphire substrates by RF reactive sputtering. The diameter and surface density of the nanocolumns depend strongly on the buffer layer, indicating that the nucleation process governs the nanostructure formation. Only the use of bs-AlN buffer layer leads to almost compact films with improved crystalline quality in terms of mosaicity (FWHM of the (0002) x-ray diffraction rocking curve = 1.2°). The broadening of the rocking curve when decreasing the column diameter is attributed to an increase of the tilt of the nanocolumns. Regarding the optical properties at room temperature, an optical absorption edge within the range of 1.71 ± 0.04 eV, and a PL emission peak at 1.59 ± 0.08 eV were observed for all the samples. The optical characteristics are determined mainly by the high residual carrier concentration. The obtained results open the possibility of using a low-cost technique like RF sputtering to develop InN nanostructures, with potential application in chemical and optical sensors.

Acknowledgments

Partial financial support was provided by the Spanish Government project TEC2012-37958-C02-01, the Comunidad de Madrid project S2013/MIT-2790, the Universidad de Alcalá project CCG2014/EXP-051, and the Marie Curie IEF grant “SolarIn” (#331745). Expert help of Andrés Valera (ICMM-CSIC) with some of the FESEM images is gratefully acknowledged.

References

[1] A.G. Bhuiyan, A. Hashimoto, A. Yamamoto, J. Appl. Phys. 94 (2003) 2779.
[2] J. Wu, J. Appl. Phys. 106 (2009) 011101.
[3] H. Lu, W.J. Schaff, L.F. Eastman, C.E. Stutz, Appl. Phys. Lett. 82 (2003) 1736.
[4] X. Wang, S. Che, Y. Ishitani, A. Yoshikawa, Appl. Phys. Lett. 90 (2007) 201913.
[5] D. Yamaguchi, T. Muto, Araki, Y. Nanishi, J. Cryst. Growth 311 (2009) 2780.
[6] W. Chen, S. Kuo, F. Lai, W. Lin, C. Hsiao, Thin Solid Films 529 (2013) 169.
[7] O. Briot, S. Ruffenach, M. Moret, B. Gil, Ch Giesen, M. Heuken, S. Rushworth, T. Leese, M. Succi, J. Cryst. Growth 311 (2009) 2761.
[8] S. Suihkonen, J. Sormunen, V.T. Rangel-Kuoppa, H. Koskenvaara, M. Sopanen, J. Cryst. Growth 291 (2006) 8.
[9] S. Ruffenach, M. Moret, O. Briot, B. Gil, Appl. Phys. Lett. 95 (2009) 042102.
[10] C.S. Gallinat, G. Koblmüller, J.S. Brown, J.S. Speck, J. Appl. Phys. 102 (2007) 064907.
[11] S. Valdueza-Felip, F.B. Naranjo, M. González-Herráez, L. Lahourcade, E. Monroy, S. Fernández, J. Cryst. Growth 312 (2010) 2689.
[12] Q. Guo, M. Ogata, Y. King, T. Tanaka, M. Nishio, J. Cryst. Growth 311 (2009) 2783.
[13] W.Z. Shen, L.F. Jiang, H.F. Yang, F.Y. Meng, H. Ogawa, Q.X. Guo, Appl. Phys. Lett. 80 (2002) 2063.
[14] Q. Guo, N. Shingai, M. Nishio, H. Ogawa, J. Cryst. Growth 189/190 (1998) 466.
[15] O. Esteban, F.B. Naranjo, N. Díaz-Herrera, S. Valdueza-Felip, M.-C. Navarrete, A. González-Cano, Sens. Actuators B 158 (2011) 372.
[16] N.C. Zoita, C. Besleaga, L. Braic, T. Mitran, C. Grigorescu, L. Nedelcu, Optoelectron. Adv. Mat 11 (2008) 719.
[17] S. Fernández, A. Martínez-Steele, J.J. Gandía, F.B. Naranjo, Thin Solid Films 517 (2009) 3152.
[18] H. Lu, William J. Schaff, J. Hwang, H. Wu, G. Koley, L.F. Eastman, Appl. Phys. Lett. 79 (2001) 1489.
[19] T.J. Kistenmacher, S.A. Ecelberger, W.A. Bryden, J. Appl. Phys. 74 (1993) 1684.
[20] J. Grandal, M.A. Sánchez-García, J. Cryst. Growth 278 (2005) 373.
[21] R. Walther, D. Litvinov, M. Fotouhi, R. Schneider, D. Gerthsen, R. Vöhringer, D. Z. Hu, D.M. Schaadt, J. Cryst. Growth 340 (2012) 34.
[22] L. Monteagudo-Lerma, S. Valdueza-Felip, A. Núñez-Cascajero, M. González-Herráez, E. Monroy, F.B. Naranjo, Thin Solid Films 545 (2013) 149.
[23] S. Valdueza-Felip, J. Ibáñez, E. Monroy, M. González-Herráez, L. Artús, F. B. Naranjo, Thin Solid Films 520 (2012) 2805.
[24] I. Horcas, R. Fernandez, J.M. Gomez-Rodriguez, J. Colchero, J. Gomez-Herrero, A.M. Baro, Rev. Sci. Instrum. 78 (2007) 013705.
[25] M. Clement, E. Iborra, J. Sangrador, A. Sanz-Hervás, L. Vergara, M. Aguilar, J. Appl. Phys. 94 (2003) 1495.

Please cite this article as: L. Monteagudo-Lerma, et al., Journal of Crystal Growth (2015), http://dx.doi.org/10.1016/j.jcrysgro.2015.10.016

UNCORRECTED PROOF

ARTICLE IN PRESS

[26] E. Dimakis, K. Tsagaraki, E. Iliopoulos, Ph Komninou, Th Kehagias, A. Delimitis, A. Georgakilas, J. Cryst. Growth 278 (2005) 367.
[27] H.M. Ng, R. Liu, F. Ponce, Proc.-Electrochem. Soc. (2004) **372**.
[28] I. Vurgaftman, J.R. Meyer, J. Appl. Phys. 94 (2003) 3675.
[29] M.A. Moram, M.E. Vickers, Rep. Prog. Phys. 72 (2009) 036502.
[30] A.U. Sheleg, V.A. Savastenko, Izv. Akad. Nauk SSSR. Neorg. Mater. 15 (1979) 1598.
[31] K. Kim, W. Lambrecht, B. Segall, Phys. Rev. B 53 (1996) 16310.
[32] K. Wang, R.R. Reeber, Appl. Phys. Lett. 79 (2001) 1602.
[33] L. Dong, S.P. Alpay, J. Mater. Sci. 47 (2012) 7587.
[34] K.S.A. Butcher, T.L. Tansley, Superlatt. Microstruct. 38 (2005) 1.
[35] Q.X. Guo, T. Tanaka, M. Nishio, H. Ogawa, X.D. Pu, W.Z. Shen, Appl. Phys. Lett. 86 (2005) 231913.
[36] W.Z. Shen, L.F. Jiang, H.F. Yang, F.Y. Meng, H. Ogawa, Q.X. Guo, Appl. Phys. Lett 80 (2002) 2063.
[37] J. Wu, W. Walukiewicz, S.X. Li, R. Armitage, J.C. Ho, E.R. Weber, E.E. Haller, H. Lu, W.J. Schaff, A. Barcz, R. Jakiela, Appl. Phys. Lett. 84 (2004) 2805.
[38] B. Liu, Z. Zhang, R. Zhang, D.Y. Fu, Z.L. Xie, H. Lu, W.J. Schaff, L.H. Song, Y.C. Cui, X.M. Hua, P. Han, Y.D. Zheng, Y.H. Chen, Z.G. Wang, Appl. Phys. A 99 (2010) 139.
[39] H. Sekiguchi, K. Kishino, A. Kikuchi, Appl. Phys. Lett. 96 (2010) 231104.

UNCORRECTED PROOF